# Charge-Lattice Coupling in Hole-Doped $LuFe_2O_{4+\delta}$: The Origin of Second-Order Modulation

Shiqing Deng,[1,2] Lijun Wu,[2] Hao Cheng,[3] Jin-Cheng Zheng,[3] Shaobo Cheng,[1,2] Jun Li,[2] Wenbin Wang,[4] Jian Shen,[5] Jing Tao,[2] Jing Zhu,[1,*] and Yimei Zhu[2,†]

[1]*School of Materials Science and Engineering, Tsinghua University, Beijing 100084, People's Republic of China*
[2]*Condensed Matter Physics and Materials Science Department, Brookhaven National Laboratory, Upton, New York 11973, USA*
[3]*Department of Physics, Xiamen University, Xiamen 361005, People's Republic of China*
[4]*Institute of Nanoelectronic Devices and Quantum Computing, Fudan University, Shanghai 200433, People's Republic of China*
[5]*Department of Physics, Fudan University, Shanghai 200433, People's Republic of China*

(Received 27 July 2018; revised manuscript received 20 January 2019; published 27 March 2019)

Understanding singularities in ordered structures, such as dislocations in lattice modulation and solitons in charge ordering, offers great opportunities to disentangle the interactions between the electronic degrees of freedom and the lattice. Specifically, a modulated structure has traditionally been expressed in the form of a discrete Fourier series with a constant phase and amplitude for each component. Here, we report atomic scale observation and analysis of a new modulation wave in hole-doped $LuFe_2O_{4+\delta}$ that requires significant modifications to the conventional modeling of ordered structures. This new modulation with an unusual quasiperiodic singularity can be accurately described only by introducing a well-defined secondary modulation vector in both the phase and amplitude parameter spaces. Correlated with density-functional-theory (DFT) calculations, our results reveal that those singularities originate from the discontinuity of lattice displacement induced by interstitial oxygen in the system. The approach of our work is applicable to a wide range of ordered systems, advancing our understanding of the nature of singularity and modulation.

DOI: 10.1103/PhysRevLett.122.126401

Symmetry breaking in quantum states is one of the central topics in modern condensed matter physics and is widely considered to be the driving force of emergent properties such as high-temperature superconductivity (HTSC), colossal magnetoresistance, and topological behavior [1–6]. Often, symmetry breaking in quantum states results in electronic and lattice modulation, e.g., charge and/or spin density wave [7,8], charge order (CO) [9], and periodic lattice displacement (PLD) [10]. It is well known that the characterization of those modulations plays a key role in the extensive research endeavor of exploring quantum states and establishing a structure-property relationship in correlated materials [10–12]. Because of the intimate coupling among charge, spin, orbital, and lattice, modulations in quantum states can be very complicated, challenging the existing methodology for both probing and comprehending their nature [1,4]. In particular, modulations in crystals arise from not only periodicity but also discreteness in the arrangements of constituent electrons and ions. Lacking accurate description of the modulation would lead to an incomplete understanding, preventing us from delving into the underlying physics.

Mathematically, collective phenomena of many quantum states or a structural modulation can be depicted by a complex order parameter, which is usually expressed as a wave function that can be expanded in the form of a discrete Fourier series [13–15]. In general, the phase and amplitude for each Fourier component are all constants regardless of whether the wave periodicity is commensurate or incommensurate [13–16]. The simplest case of a wave with single wave vector $\mathbf{q}$ is illustrated in Fig. 1(a) for a one-dimensional modulation. Increasing dimensions in the wave vector space (multiple $\mathbf{q}$) only adds independent Fourier components, leaving the phase and amplitude of each $\mathbf{q}$ vector constant [13]. Nevertheless, in reality, a long-range modulation can be easily disrupted by singularities in the material, which could come from defects in the crystal lattice, like edge dislocation and antiphase boundary [17,18], and/or discontinuities in electronic structures, e.g., extra charge localization at individual ions [12,19–21]. Consequently, the constant phase and amplitude in the modulation wave can be broken, which induces variations, such as topological phase defects and solitons [12,20–23]. A singularity in the phase of modulations, i.e., a phase shift, is presented in Fig. 1(b). Those singularities may vary the correlation length (e.g., forming domains depending on the dimensionality) and can substantially modify physical properties [24]. The distribution of phase singularities can be random or periodic in real space as a result of competing energies in the system. In the case of periodically distributed phase singularities, a new wave vector $\mathbf{q}$ can be given for singularities in addition to the wave vector $\mathbf{q}$ of the modulation. These two $\mathbf{q}$ vectors are in principle independent; however, to date, only one

 

experimental observation has been reported for a case with two $\mathbf{q}$ vectors along the same direction, and the modulation amplitude remains unchanged [20]. All the above works suggest that modulations may exist with additional degrees of freedom in both phase and amplitude parameter spaces in a variety of materials. Understanding these modulations would advance our knowledge on the structural origin of properties, and the modified phase and amplitude may assist in the interpretation of the entanglement in quantum materials.

In this Letter, we present a study of an emergent modulation in a hole-doped CO system $LuFe_2O_{4+\delta}$ ($\delta$ is around 0.15) using advanced scanning transmission electron microscopy (STEM). The finding is schematically illustrated in Fig. 1(c); i.e., the phase and amplitude are characterized to be associated with a well-defined secondary wave, being a function of the second-order modulation vector ($\mathbf{q_s}$) and position vector ($\mathbf{r}$). Indeed, this can be considered as a universal expression of an order parameter, which might be applicable to diverse ordered systems. Insight from this work may also shed light on deciphering how the doped holes entangle with charge and lattice that determines many emergent quantum states in materials.

$LuFe_2O_4$ is a model system with room-temperature CO. It has triangular bilayers of $FeO_5$ bipyramids sandwiched between Lu-O layers along the $\mathbf{c}$ direction [Fig. 2(a)] and space group $R\bar{3}m$ [25–27]. An equal amount of $Fe^{2+}$ and $Fe^{3+}$ ions on the triangular lattice forms the charge

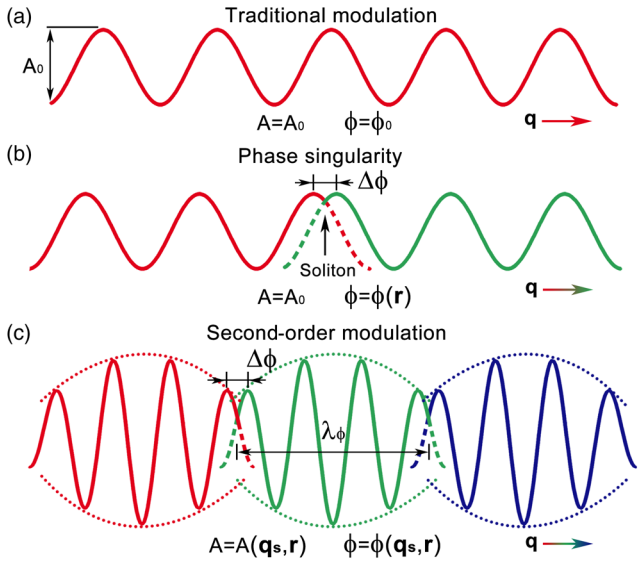


FIG. 1. Illustrations of different types of modulation. (a) Traditional modulation (single wave vector $\mathbf{q}$). Both phase ($\phi_0$) and amplitude ($A_0$) are constants. (b) A singularity in the modulation phase, i.e., a phase shift ($\Delta\phi$), generates phase variations with position vector ($\mathbf{r}$). (c) Second-order modulation. Phase and amplitude are modulated by a secondary wave, being a function of second-order modulation wave vector ($\mathbf{q_s}$) and position vector ($\mathbf{r}$).

frustration due to energy degeneracy [28], depending on the excess of electron or hole on the third triangular corner [Fig. 2(a), lower panel]. This arrangement makes its ground states highly susceptible to charge fluctuations, composition, and temperature, leading to structural flexibility and chemical sensitivity [29–31]. Many interesting diffraction patterns have been observed and a series of intermediate states can be obtained upon doping [29–32], which therefore make it a very suitable platform for achieving and exploring emergent modulations.

Figure 2(b) shows an electron diffraction pattern (EDP) along the [100] zone axis of the hole-doped $LuFe_2O_{4+\delta}$. Apart from fundamental spots, a constellation of satellite reflections that are absent in the stoichiometric sample ($\delta = 0$, Fig. S1 [33]) is observed, suggesting a modulated structure. Detailed inspections of EDP [Fig. 2(c)] reveal that sharp satellite reflections align well along the $\mathbf{g_1} = [027]^*$ direction [we hereafter refer to this as primary modulation (PM) spots, indexed as $(hkl, m_1, 0)$], which can be characterized by an incommensurate modulation wave vector $\mathbf{q_p}$ ($\sim 0.135\mathbf{g_1}$). Importantly, it is noted that each PM spot is accompanied by a second-order modulation (SOM) spot [indexed as $(hkl, m_1, m_2)$ with $m_1 = m_2 = \pm 1$] running along the $\mathbf{g_2} = [01\bar{7}]^*$ direction, marked as $\mathbf{q_s}$ ($\sim 0.110\mathbf{g_2}$) in Fig. 2(c). This scenario manifests a marked difference from the traditional two-dimensional modulation [13,15,16], where two sets of first-order modulation spots appear both around fundamental spots.

To unravel this emergent modulation, quantitative analysis of the atomically resolved high-angle annular dark-field (HAADF) STEM image [Fig. 2(e)] was conducted using a peak-pair algorithm (Supplemental Material Part 1 [33]) [39]. PLD maps of Lu along vertical [001] [Fig. 2(f)] and horizontal [120] directions (Fig. S2 [33]) were acquired. The most prominent feature is that the stripes of positive and negative displacement alternatively distribute along the $[027]^*$ direction, yielding a periodicity of around 10 Å, consistent with PM spots ($\lambda = 1/|\mathbf{q_p}| \approx 10.2$ Å). Displacement vectors in Fig. 2(g) follow a serpentine curve along the $\mathbf{q_p}$ direction, which generates a sinusoidal PM wave as demonstrated in the displacement line profile [Fig. 2(h)]. It is noteworthy that in PLD maps [Fig. 2(f) herein and Fig. S2 in Supplemental Material [33]] positive and negative displacement stripes are not well aligned but periodically glide along the $(01\bar{7})$ plane, indicated by the white dashed lines. Its periodicity is about 20 Å, which is consistent with SOM spots ($\lambda_s = 1/|\mathbf{q_s}| \approx 20.89$ Å). As revealed by the line trace [Fig. 2(h)], this glide is caused by the singularity in the PM wave phase, i.e., a phase shift, $\Delta\phi = 2\pi d/\lambda \approx 0.17(2\pi)$. Periodic singularities generate a modulated phase along the $\mathbf{q_s}$ direction, yielding a SOM. The same observation is reproduced by rotating the scanning direction 90 deg during the image acquisition (Fig. S3 [33]), thus ruling out the possible artifacts. Further inspections of PLD maps and line profiles reveal that the

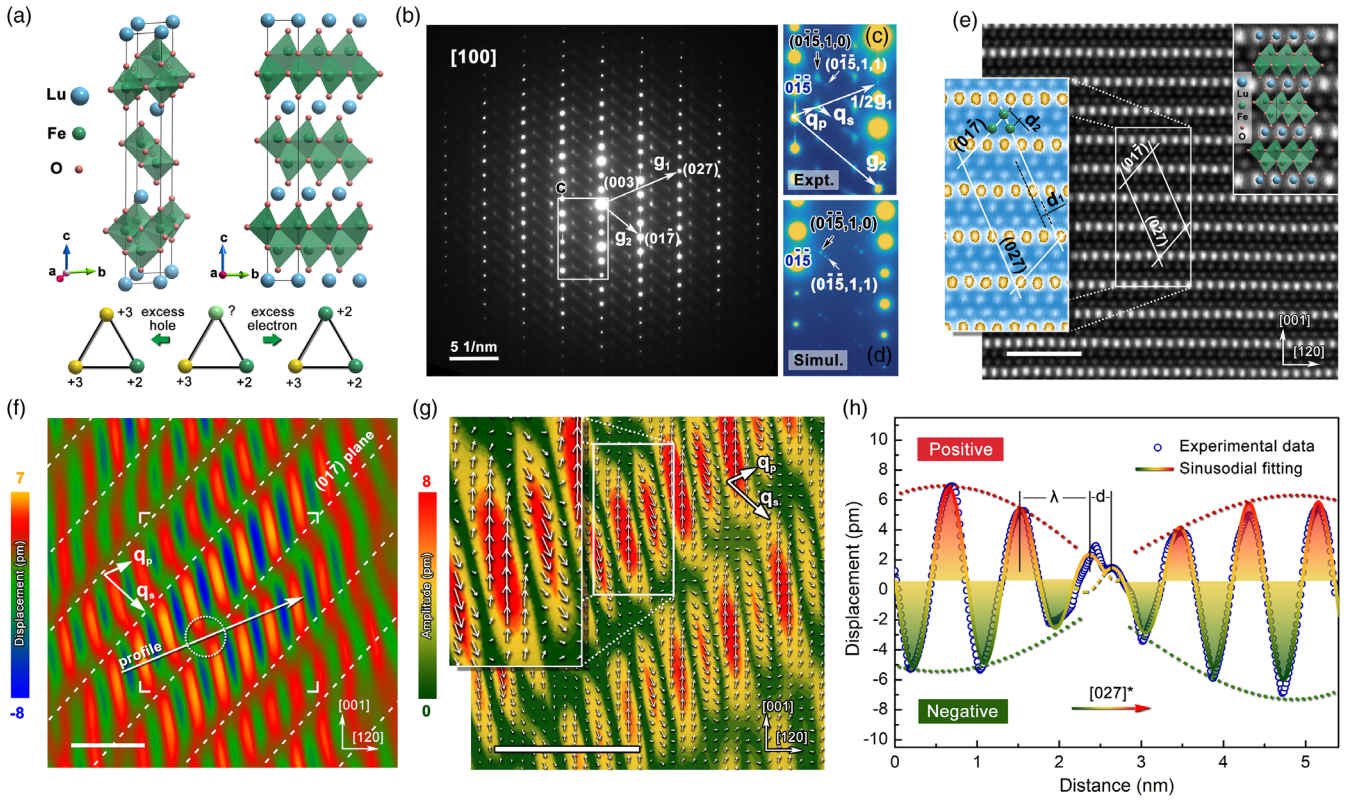


FIG. 2. Second-order incommensurate modulation. (a) The left-hand side of the upper panel demonstrates the three-dimensional rhombohedral structure of $LuFe_2O_4$, and its projection along the **a** axis is shown on the right-hand side. Lower panel illustrates charge frustration. (b) [100] zone axis EDP with a series of satellite reflections. (c) Close-up of region marked in (b). Two vectors, $\mathbf{q_p}$ ($\sim 0.135\mathbf{g_1}$) and $\mathbf{q_s}$ ($\sim 0.110\mathbf{g_2}$), are assigned for PM and SOM spots, respectively. (d) Simulated EDP considering both PM and SOM [Eq. (2)]. The fourth ($m_1$) and fifth ($m_2$) index correspond to $\mathbf{q_p}$ and $\mathbf{q_s}$, respectively. (e) HAADF-STEM image along the **a** axis. Spacings of the parallelogram correspond to real-space distances of $\mathbf{q_p}$ and $\mathbf{q_s}$. $d_1$ and $d_2$ are (027) and $(01\bar{7})$ planar distance, respectively. (f) PLD map along the [001] direction. Periodic phase shift occurs at $(01\bar{7})$ planes, indicated by the broken white lines. (g) Displacement vector map of Lu extracted from delimiters-framed area in (f). An enlargement of the marked section is shown. Arrows follow displacement directions. Arrow length and color-coded background represent the amplitude. (h) Displacement line profile along $\mathbf{q_p}$ marked in (f), showing the phase shift ($\Delta\phi = 2\pi d/\lambda$) and amplitude oscillation, outlined by envelope curves. All scale bars are 2 nm.

amplitude of PM also varies with position vector ($\mathbf{r}$) and forms an oscillation, indicated by envelope curves in Fig. 2(h). The amplitude minima occur at the positions where phase singularity takes place. This situation is consistent with the previous theoretical prediction that the modulation amplitude collapses at phase deformations to prevent divergence of energy density [40,41].

In general, PLDs can be depicted by a complex order parameter, which can be mathematically expanded in the form of a discrete Fourier series with a constant phase and amplitude for each component [13–16]. Traditionally, for a double-$\mathbf{q}$ case ($\mathbf{q_1}$, $\mathbf{q_2}$), the displacement ($\mathbf{u}$) of atom $\mu$ can be represented by

$$\mathbf{u}(\mu, \mathbf{r}^\mu) = \mathbf{A}_1^\mu \sin[2\pi(\mathbf{q_1}\cdot\mathbf{r}^\mu + \phi_1^\mu)] + \mathbf{A}_2^\mu \sin[2\pi(\mathbf{q_2}\cdot\mathbf{r}^\mu + \phi_2^\mu)]. \quad (1)$$

$\mathbf{r}^\mu = \mathbf{T} + \mathbf{r}_\mathbf{b}^\mu$ is the position vector with the lattice vector ($\mathbf{T}$) and the position of atom $\mu$ in the basic structure ($\mathbf{r}_\mathbf{b}^\mu$). $\mathbf{A_1}$, $\mathbf{A_2}$ and $\phi_1$, $\phi_2$ are amplitudes and phases for $\mathbf{q_1}$ and $\mathbf{q_2}$, respectively, which are independent and constants. In our case, although there also exist two $\mathbf{q}$ vectors ($\mathbf{q_p}$, $\mathbf{q_s}$), an attempt to describe the modulation using the above formula leads to a failure (Supplemental Material Part 2 and Fig. S4 [33]). According to experimental observations, a new type of modulation wave is defined,

$$\mathbf{u}(\mu, \mathbf{r}^\mu) = \mathbf{A}_\mathbf{p}^\mu(\mathbf{q_s}, \mathbf{r}^\mu)\ \sin\{2\pi[\mathbf{q_p}\cdot\mathbf{r}^\mu + \phi_p^\mu(\mathbf{q_s}, \mathbf{r}^\mu)]\}, \quad (2)$$

with $\mathbf{A}_\mathbf{p}^\mu(\mathbf{q_s}, \mathbf{r}^\mu) = \mathbf{B}_\mathbf{s}^\mu + \mathbf{A}_\mathbf{s}^\mu \sin[2\pi(\mathbf{q_s}\cdot\mathbf{r}^\mu + \phi_s^\mu)]$ and $\phi_p^\mu(\mathbf{q_s}, \mathbf{r}^\mu) = 0.17 \times \mathrm{Integer}(\mathbf{q_s}\cdot\mathbf{r}^\mu)$. $\mathbf{B}_\mathbf{s}^\mu$, $\mathbf{A}_\mathbf{s}^\mu$, and $\phi_s^\mu$ are constants. Compared with Eq. (1) that has Fourier terms for $\mathbf{q_1}$ and $\mathbf{q_2}$ separately, there exists only a Fourier term for PM ($\mathbf{q_p}$). More importantly, the phase and amplitude of PM are modulated by a SOM wave instead of being constants and become a function of SOM wave vector ($\mathbf{q_s}$) and position vector ($\mathbf{r}$). In this way, PM ($\mathbf{q_p}$) and SOM ($\mathbf{q_s}$) are

intertwined, and their essential nature differs from the traditional two-dimensional modulation [13]. Based on Eq. (2), systematic simulations using the Bloch-wave method can well reproduce experimental observations in both reciprocal and real space (Fig. 2(d) herein and Fig. S4(d) in Supplemental Material [33]).

Apart from this harmonious SOM, randomly distributed nascent topological defects, like phase dislocations, were also observed (Fig. S5 [33]). Such phase defects have been previously reported in, e.g., charge-ordered manganites [12,21,24], which could come from impurities, elastic strain, and/or discontinuities in electronic structures [41,42]. Serving as pinning centers, they can break the long-range ordering of SOM, which accounts for the diffuse nature of SOM spots in our experiments.

As the PLDs are essentially generated by the modulation of charge density via charge-lattice coupling, this SOM has its origin in the abnormal charge distributions caused by doped holes. The hole doping nature was confirmed in Fig. S6 [43]. Charge modulation was further attested using atomically resolved electron energy-loss spectroscopy (EELS). It is well known that features of $L_{2,3}$ edges, including shape [47], position [48,49], and $L_3/L_2$ ratio [34,50], serve as fingerprints for the transition metals' valency. Spectroscopic data of Fe-$L_{2,3}$ edges and the HAADF-STEM image were simultaneously acquired pixel by pixel [Fig. 3(a), inset]. The spectrum image clearly shows the atomic Fe sublattice, manifesting the high spatial resolution achieved to investigate individual Fe columns. Figure 3(a) demonstrates three postprocessed Fe-$L_{2,3}$ edges from sites A–C. Since the higher energy of the edge onset and the $L_3/L_2$ ratio for Fe correspond to higher oxidation states (below $Fe^{3+}$) [34,49,50], the valence increases monotonically from site C to site A. We then extracted all $L_3/L_2$ ratios, color coded and overlaid on the Fe sublattice [Fig. 3(b)]. Clear charge oscillations are visualized, which can be well fitted by a series of (027) and $(01\bar{7})$ planes with a periodic phase shift ($\Delta\phi$). The integration of $L_3/L_2$ ratios at each (027) plane along the $\mathbf{q_p}$ direction [Fig. 3(c)] further confirms such a phase shift, yielding $\Delta\phi \approx 0.20(2\pi)$. This is consistent with structural modulation wave [Fig. 2(h)] and diffraction calculations [Fig. S4(d) [33]]. We note that measurements of $L_3/L_2$ ratios have rather large error bars, which may come from the well-documented effects, such as inelastic delocalization and probe broadening [51–53]. Deviation from the model may be related to the small imperfection of the area and/or the random error in measurement. These observations manifest the quasiperiodic singularity in the phase of charge modulation, which accounts for the discontinuities of PLDs and can also be well described by the SOM defined in Eq. (2).

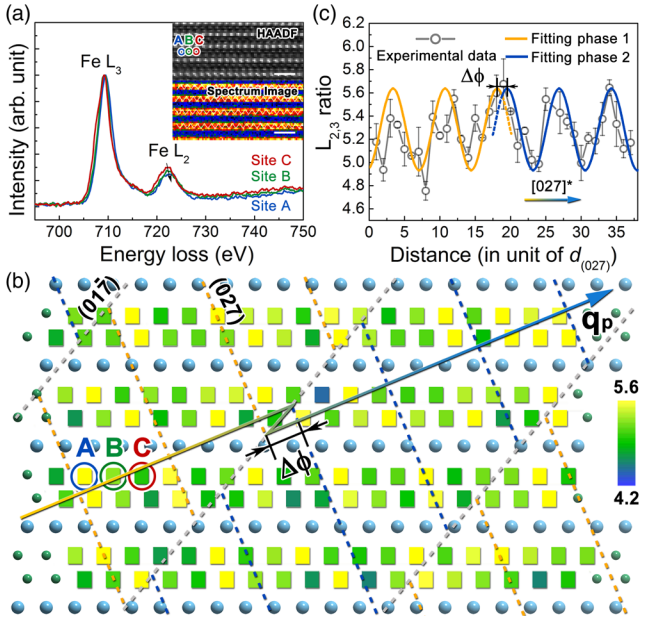


FIG. 3. EELS characterizations showing charge discontinuity. (a) EELS spectra at sites A–C extracted from the atomically resolved spectrum image of Fe-$L_{2,3}$ edges in the inset. (b) Color-coded Fe-$L_3/L_2$ ratios extracted from each atomic column in spectrum image. Mesh spacings correspond to real-space distances of $\mathbf{q_p}$ and $\mathbf{q_s}$. (c) Integration of $L_3/L_2$ ratios at each (027) plane at the arrow position in (b). Experimental data can be fitted by two sinusoidal waves with a phase shift ($\Delta\phi$). Scale bars are 1 nm.

Previous studies on HTSCs suggested that local structural features and changes in carrier density for superconductivity depend on interstitial oxygens ($O_i$) [10]. Therefore, to unravel the origin of this charge-lattice SOM, the most stable $O_i$ position in the $LuFe_2O_{4+\delta}$ unit cell was determined by DFT calculations (Supplemental Material Part 3) [54]. Because of the **c**-axial layered structure, considering possible interstitial sites in one stacking block is sufficient (Fig. S7 [54]). Typical interstitial sites are labeled with A–E in the **a**-**b** plane [Fig. 4(a), left-hand panel] and each with different $z$ positions, indicated by vertical lines (right-hand panel). For each site, ground state energies are calculated as a function of $z$ position and the potential-energy surface is obtained [Fig. 4(b)]. To minimize the influence of $O_i$-$O_i$ coupling, we take the lowest energy as reference and compare the relative total energy. It is found that site A is energetically favorable for all $z$ positions due to the largest void volume. Among all the A sites (different $z$ positions), one particular site, denoted as site $A_0$ ($z/c = 0.7816$), has the shortest Fe–$O_i$ bond length and the lowest energy. Importantly, this site resides right at the junction of two edge-sharing planes of $FeO_5$ cages [Fig. 4(b), inset], which is the intersection of the (027) and $(01\bar{7})$ planes.

Combing the calculations with experiments, a possible mechanism for SOM is proposed [Fig. 4(c)]. Based on PLD and charge mapping results, a mesh consisting of a series of (027) and $(01\bar{7})$ planes was drawn to translate (027) planes passing through the lowest-energy $O_i$. Since ionic

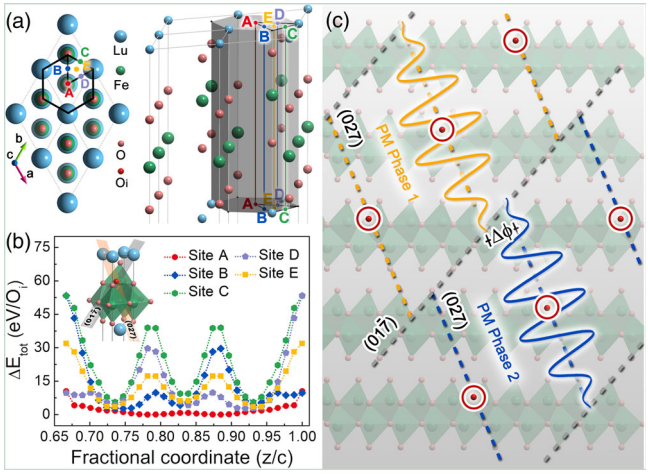


FIG. 4. DFT calculations on the origin of SOM. (a) Five isolated interstitial sites considered in calculations, indexed from A to E in the **a**-**b** plane (left-hand panel). Each site consists of a series of $z$ positions, indicated by vertical lines (right-hand panel). (b) The relative total energies (eV/$O_i$) as a function of the fractional coordinate. Polyhedron exhibits the lowest-energy site (site $A_0$) with $z/c = 0.7816$. (c) A schematic illustrating the charge-lattice SOM. $O_i$ resides at the lowest-energy site based on calculations. Lutetium is omitted for clarity. The discontinuity of displacement magnitude-damping curves (blue and yellow) induces the phase glide ($\Delta\phi$).

displacements are essentially caused by $O_i$, their magnitude reaches a maximum at the $O_i$ site and damps down with the increase in distance. Consequently, it yields periodic displacement damping curves (yellow for phase 1, blue for phase 2) along the (027) plane. As two damping curves cannot merge at the $(01\bar{7})$ plane, a glide operation forms that generates phase discontinuities and amplitude oscillations in the PM. Meanwhile, local electronic structure and charge density are also modified by $O_i$, as revealed by EELS results. In this picture, interstitial oxygens serving as solitons bring singularities in both lattice and charge modulations, which is analogous to the case in hole-doped cuprates [20]. Periodic singularities introduce a secondary order into the PM phase and amplitude along the $\mathbf{q_s}$ direction. Meanwhile, a new periodicity for $(01\bar{7})$ planes related to SOM spots forms. Eventually, the PM phase and amplitude are modulated by a SOM wave and are dependent on the SOM wave vector $\mathbf{q_s}$ and position vector $\mathbf{r}$, leading to intertwined PM and SOM, as defined in Eq. (2).

The distribution of singularities in modulation can be random [12,21] or periodic in real space (this study) as a result of competing energies in the system. On the basis of our experimental observations, DFT calculations, and simulations, we propose a new paradigm of modulating phase and amplitude parameter spaces by a second-order wave ($\mathbf{q_s}$). As illustrated in the modulation formula [Eq. (2)], a $\mathbf{q}$ vector (e.g., $\mathbf{q_2} = \mathbf{q_s}$) is introduced into the phase and amplitude field $[\mathbf{u} = \mathbf{u_1}[\mathbf{q_1}, \mathbf{A_1}(\mathbf{q_2}), \phi_1(\mathbf{q_2})]]$ rather than as an independent Fourier component $[\mathbf{u} = \mathbf{u_1}(\mathbf{q_1}) + \mathbf{u_2}(\mathbf{q_2})]$ [13]. This concept is readily generalizable to multiple-$\mathbf{q}$ cases. The phase and amplitude for all Fourier components can be independently modulated by a second-order wave ($\mathbf{q_s^j}$), i.e., $\mathbf{u} = \sum_{i,j} \mathbf{u}_i[\mathbf{q}_i, \mathbf{A}_i(\mathbf{q_s^j}), \phi_i(\mathbf{q_s^j})]$. Based on this framework, additional degrees of freedom are essentially added in both phase and amplitude parameter spaces. This formulism provides a more accurate and universal depiction of the order parameter and can be widely applicable to numerous ordered systems, as singularities are ubiquitous [12,21–24,42].

In summary, by purposely introducing excess holes in a prototype charge-ordered system $LuFe_2O_{4+\delta}$, we observed a new type of modulation with its phase and amplitude modulated by a second-order modulation wave using state-of-the-art electron microscopy. By directly measuring lattice and charge components at atomic scale, quasiperiodic singularities are found in both periodic lattice displacements and charge modulation. We show that due to the interplay between interstitial oxygens, lattice locking, and charge frustration, the phase and amplitude of primary modulation can be tuned by quasiperiodic singularities, engendering a second-order modulation wave. Through introducing a $\mathbf{q}$ vector into amplitude and phase parameter spaces, a new modulation formulism is developed. Our study illustrates a new approach to manipulate singularity in modulation waves via targeted hole doping to understand the intriguing behavior of quantum materials.

The electronic microscopy study was carried out at Brookhaven National Laboratory and supported by the U.S. DOE Basic Energy Sciences, Materials Sciences and Engineering Division under Contract No. DESC0012704. J. Z., S. D., and S. C. would like to acknowledge the financial support by Chinese National Natural Science Foundation under Project No. 51390471 and the National 973 Project of China (Project No. 2015CB654902) as well as the support of S. D. for studying abroad from China Scholarship Council. This work made use of the resources of the National Center for Electron Microscopy in Beijing. The theoretic work was done at Xiamen University. The research at Fudan University was supported by National Key Research and Development Program of China (Grant No. 2016YFA0300702), National Natural Science Foundation of China (Grant No. 11504053), Program of Shanghai Academic Research Leader (Grant No. 17XD1400400), and National Key Research and Development Program of China (Grant No. 2016YFA0300702). We thank Wei Wang for very helpful discussion and help on the quantitative analysis of electron microscopy images.

*Corresponding author.
jzhu@mail.tsinghua.edu.cn
†Corresponding author.
zhu@bnl.gov

[1] E. Dagotto, Science **309**, 257 (2005).

[2] H. Alloul, J. Bobroff, M. Gabay, and P. J. Hirschfeld, Rev. Mod. Phys. **81**, 45 (2009).
[3] G. Ghiringhelli *et al.*, Science **337**, 821 (2012).
[4] J. Chang *et al.*, Nat. Phys. **8**, 871 (2012).
[5] X.-L. Qi and S.-C. Zhang, Rev. Mod. Phys. **83**, 1057 (2011).
[6] P. W. Anderson, *Basic Notions of Condensed Matter Physics* (CRC Press, Boca Raton, FL, 1997).
[7] T. Ritschel, J. Trinckauf, K. Koepernik, B. Büchner, M. v. Zimmermann, H. Berger, Y. I. Joe, P. Abbamonte, and J. Geck, Nat. Phys. **11**, 328 (2015).
[8] H. v. Löhneysen, A. Rosch, M. Vojta, and P. Wölfle, Rev. Mod. Phys. **79**, 1015 (2007).
[9] U. Staub, G. I. Meijer, F. Fauth, R. Allenspach, J. G. Bednorz, J. Karpinski, S. M. Kazakov, L. Paolasini, and F. d'Acapito, Phys. Rev. Lett. **88**, 126402 (2002).
[10] Y. Gao, P. Lee, P. Coppens, M. A. Subramanian, and A. W. Sleight, Science **241**, 954 (1988).
[11] R. Comin *et al.*, Nat. Mater. **14**, 796 (2015).
[12] B. H. Savitzky, I. El Baggari, A. S. Admasu, J. Kim, S. W. Cheong, R. Hovden, and L. F. Kourkoutis, Nat. Commun. **8**, 1883 (2017).
[13] A. J. C. Wilson and E. Prince, *International Tables for Crystallography*, Vol. C: Mathematical, Physical and Chemical Tables, 2nd ed. (Kluwer Academic Publishers, Dordrecht, 1999), pp. 899–907.
[14] P. M. de Wolf, Acta Crystallogr. Sec. A **33**, 493 (1977).
[15] J. M. Perez-Mato, G. Madariaga, F. J. Zuñiga, and A. Garcia Arribas, Acta Crystallogr. Sect. A **43**, 216 (1987).
[16] A. Yamamoto, Acta Crystallogr. Sec. A **38**, 87 (1982).
[17] D. T. Margulies, F. T. Parker, M. L. Rudee, F. E. Spada, J. N. Chapman, P. R. Aitchison, and A. E. Berkowitz, Phys. Rev. Lett. **79**, 5162 (1997).
[18] T. Hibma, F. C. Voogt, L. Niesen, P. A. A. van der Heijden, W. J. M. de Jonge, J. J. T. M. Donkers, and P. J. van der Zaag, J. Appl. Phys. **85**, 5291 (1999).
[19] W. L. McMillan, Phys. Rev. B **14**, 1496 (1976).
[20] C. Guo, H. F. Tian, H. X. Yang, B. Zhang, K. Sun, X. Sun, Y. Y. Peng, X. J. Zhou, and J. Q. Li, Phys. Rev. Mater. **1**, 064802 (2017).
[21] I. El Baggari, B. H. Savitzky, A. S. Admasu, J. Kim, S. W. Cheong, R. Hovden, and L. F. Kourkoutis, Proc. Natl. Acad. Sci. U.S.A. **115**, 1445 (2018).
[22] W. S. Lee *et al.*, Nat. Commun. **3**, 838 (2012).
[23] P. Zhu *et al.*, Appl. Phys. Lett. **103**, 071914 (2013).
[24] J. Tao, K. Sun, W.-G. Yin, L. Wu, H. Xin, J. G. Wen, W. Luo, S. J. Pennycook, J. M. Tranquada, and Y. Zhu, Sci. Rep. **6**, 37624 (2016).
[25] M. Isobe, N. Kimizuka, J. Iida, and S. Takekawa, Acta Crystallogr. Sect. C **46**, 1917 (1990).
[26] Y. Zhang, H. X. Yang, Y. Q. Guo, C. Ma, H. F. Tian, J. L. Luo, and J. Q. Li, Phys. Rev. B **76**, 184105 (2007).
[27] N. Ikeda *et al.*, Nature (London) **436**, 1136 (2005).
[28] Y. Yamada, K. Kitsuda, S. Nohdo, and N. Ikeda, Phys. Rev. B **62**, 12167 (2000).
[29] M. Hervieu, A. Guesdon, J. Bourgeois, E. Elkaim, M. Poienar, F. Damay, J. Rouquette, A. Maignan, and C. Martin, Nat. Mater. **13**, 74 (2014).
[30] S. Cao, J. Li, Z. Wang, H. Tian, Y. Qin, L. Zeng, C. Ma, H. Yang, and J. Li, Sci. Rep. **2**, 330 (2012).
[31] Y. Zhang, H. X. Yang, C. Ma, H. F. Tian, and J. Q. Li, Phys. Rev. Lett. **98**, 247602 (2007).
[32] J. de Groot, T. Mueller, R. A. Rosenberg, D. J. Keavney, Z. Islam, J.-W. Kim, and M. Angst, Phys. Rev. Lett. **108**, 187601 (2012).
[33] See Supplemental Material at http://link.aps.org/supplemental/10.1103/PhysRevLett.122.126401 for details of experiments, quantitative analysis, and simulations, which include Refs. [13,34–38].
[34] P. A. van Aken and B. Liebscher, Phys. Chem. Miner. **29**, 188 (2002).
[35] J. Mayer, L. Giannuzzi, T. Kamino, and J. Michael, MRS Bull. **32**, 400 (2007).
[36] K. Thompson, B. Gorman, D. J. Larson, B. van Leer, and L. Hong, Microsc. Microanal. **12**, 1736 (2006).
[37] Z. Huang, J. Microsc. **215**, 219 (2004).
[38] P. L. Galindo, S. Kret, A. M. Sanchez, J. Y. Laval, A. Yanez, J. Pizarro, E. Guerrero, T. Ben, and S. I. Molina, Ultramicroscopy **107**, 1186 (2007).
[39] P. Galindo, J. Pizarro, S. Molina, and K. Ishizuka, Microsc. Anal. **130**, 23 (2009).
[40] D. Feinberg and J. Friedel, J. Phys. (Paris) **49**, 485 (1988).
[41] S. N. Coppersmith and A. J. Millis, Phys. Rev. B **44**, 7799 (1991).
[42] J. Tao, K. Sun, J. M. Tranquada, and Y. Zhu, Phys. Rev. B **95**, 235113 (2017).
[43] See Supplemental Material at http://link.aps.org/supplemental/10.1103/PhysRevLett.122.126401 for EELS spectra analysis, which includes Refs. [44–46].
[44] R. F. Egerton, *Electron Energy-Loss Spectroscopy in the Electron Microscope*, 3rd ed. (Springer Science and Business Media, LLC, New York, NY, 2011).
[45] L. A. Grunes, R. D. Leapman, C. N. Wilker, R. Hoffmann, and A. B. Kunz, Phys. Rev. B **25**, 7157 (1982).
[46] J. A. Mundy, Q. Mao, C. M. Brooks, D. G. Schlom, and D. A. Muller, Appl. Phys. Lett. **101**, 042907 (2012).
[47] J. H. Paterson and O. L. Krivanek, Ultramicroscopy **32**, 319 (1990).
[48] M. T. Otten, B. Miner, J. H. Rask, and P. R. Buseck, Ultramicroscopy **18**, 285 (1985).
[49] H. Tan, J. Verbeeck, A. Abakumov, and G. Van Tendeloo, Ultramicroscopy **116**, 24 (2012).
[50] S. Deng, S. Cheng, C. Xu, B. Ge, X. Sun, R. Yu, W. Duan, and J. Zhu, ACS Appl. Mater. Interfaces **9**, 27322 (2017).
[51] L. J. Allen, S. D. Findlay, M. P. Oxley, C. Witte, and N. J. Zaluzec, Ultramicroscopy **106**, 1001 (2006).
[52] H. Tan, S. Turner, E. Yücelen, J. Verbeeck, and G. Van Tendeloo, Phys. Rev. Lett. **107**, 107602 (2011).
[53] C. Mitterbauer, G. Kothleitner, W. Grogger, H. Zandbergen, B. Freitag, P. Tiemeijer, and F. Hofer, Ultramicroscopy **96**, 469 (2003).
[54] See Supplemental Material at http://link.aps.org/supplemental/10.1103/PhysRevLett.122.126401 for details of DFT calculations, which include Refs. [55–57].
[55] P. Giannozzi *et al.*, J. Phys. Condens. Matter **21**, 395502 (2009).
[56] J. P. Perdew, K. Burke, and M. Ernzerhof, Phys. Rev. Lett. **77**, 3865 (1996).
[57] K. F. Garrity, J. W. Bennett, K. M. Rabe, and D. Vanderbilt, Comput. Mater. Sci. **81**, 446 (2014).